JACS
JOURNAL OF THE AMERICAN CHEMICAL SOCIETY
pubs.acs.org/JACS
Article

Using High-Entropy Configuration Strategy to Design Na-Ion Layered Oxide Cathodes with Superior Electrochemical Performance and Thermal Stability

Feixiang Ding, Chenglong Zhao, Dongdong Xiao, Xiaohui Rong,* Haibo Wang, Yuqi Li, Yang Yang, Yaxiang Lu,* and Yong-Sheng Hu*

Cite This: https://doi.org/10.1021/jacs.2c02353
Read Online

ACCESS | Metrics & More | Article Recommendations | Supporting Information

ABSTRACT: Na-ion layered oxide cathodes (Na_xTMO_2, TM = transition metal ion(s)), as an analogue of lithium layered oxide cathodes (such as $LiCoO_2$, $LiNi_xCo_yMn_{1-x-y}O_2$), have received growing attention with the development of Na-ion batteries. However, due to the larger Na^+ radius and stronger Na^+−Na^+ electrostatic repulsion in NaO_2 slabs, some undesired phase transitions are observed in Na_xTMO_2. Herein, we report a high-entropy configuration strategy for Na_xTMO_2 cathode materials, in which multicomponent TMO_2 slabs with enlarged interlayer spacing help strengthen the whole skeleton structure of layered oxides through mitigating Jahn−Teller distortion, Na^+/vacancy ordering, and lattice parameter changes. The strengthened skeleton structure with a modulated particle morphology dramatically improves the Na^+ transport kinetics and suppresses intragranular fatigue cracks and TM dissolution, thus leading to highly improved performances. Furthermore, the elaborate high-entropy TMO_2 slabs enhance the TM−O bonding energy to restrain oxygen release and thermal runaway, benefiting for the improvement of thermal safety.

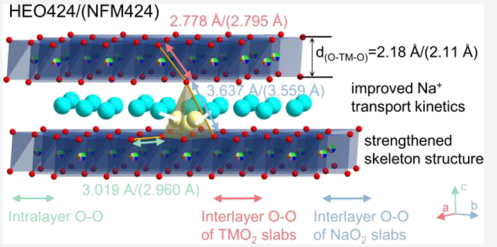

INTRODUCTION

Developing high-performance and sustainable electrochemical energy storage and conversion systems are under increasing demand for today's renewable energy applications such as smart power grids. Na-ion batteries (NIBs), due to the Na abundance and worldwide availability compared with Li, are considered as supplements of Li-ion batteries (LIBs) to fulfill this requirement.[1−3] The Na-ion layered oxide materials, with a formula of Na_xTMO_2 (TM = transition metal ion(s)), are the most promising cathode materials for NIBs due to the advantages of high energy density, easy manufacture, and low cost. However, Na_xTMO_2 cathode materials experience diverse stacking sequences and complex phase transitions compared to their Li-contained analogues, which stems from the larger Na^+ radius and stronger Na^+−Na^+ electrostatic repulsion in NaO_2 slabs.[4] Thus, the structure of Na_xTMO_2 cathodes depends heavily on the sodium content regardless of the pristine or the charged materials, bringing about different influences on electrochemical performances. In general, a high Na^+ content ($0.8 < x \leq 1.0$) allows the formation of an O3-type structure similar to $LiCoO_2$, and a slightly smaller Na^+ content of 0.4−0.8 drives the appearance of P-type structures (such as P2 and P3), in which Na^+ occupies the trigonal prismatic (P) site. However, with further desodiation to less than ∼0.4, Na^+-deficient O-type phases (O3/O2) or O/P-type coexisting phases (OP2/OP4/Z) will be formed.[5−8]

On the other hand, TMO_2 slabs (sheets of edge-sharing TMO_6 octahedra) also play an important role in determining the crystal structure and property, which not only serve as the redox center to contribute to the charge compensation but also the structural skeleton to stabilize the crystal framework. Therefore, rational compositional design in TMO_2 layers can achieve structure modulation. For instance, the substitution of Mn^{4+}/Ni^{2+} by Li^+ for P2-$Na_{2/3}Ni_{1/3}Mn_{2/3}O_2$ can form high Na-Content P2-$Na_{45/54}Li_{4/54}Ni_{16/54}Mn_{34/54}O_2$;[9] the disordered arrangement of Cr^{3+} and Ti^{4+} in the TMO_2 layers of P2-$Na_{0.6}Cr_{0.6}Ti_{0.4}O_2$[10] and substitution of Mn^{4+} by Ti^{4+} for P2-$Na_{2/3}Ni_{1/3}Mn_{1/3}Ti_{1/3}O_2$[11] can suppress Na^+/vacancy ordering, all of which displayed improved electrochemical properties. Besides the substitution in P2-type cathode materials, the adjustment of TMO_2 slabs in the O3-type structure with full Na^+ site occupation also gains unremitting efforts to optimize the structural integrity and electrochemical performance. In early studies, unitary layered TM oxides were investigated for applications in NIBs, such as $NaCrO_2$,[12] $NaFeO_2$,[13] $NaCoO_2$,[14] and $NaNiO_2$,[15] which usually experience complicated phase transitions or Na^+/vacancy ordering, thus leading to significant capacity attenuation after several cycles. Then,

Received: March 2, 2022

binary TM oxides (e.g., $NaNi_{0.5}Mn_{0.5}O_2$) were explored, and even though slightly encouraging results were obtained; phase transitions among O3, O'3, P3 and P'3 during charge still appear, causing deteriorated cycle performance.[6] Subsequently, multi-substitution was tried; for instance, the substitution of Mn^{4+} by Sn^{4+} or Ti^{4+}, dual substitution of Ni^{2+} and Mn^{4+} by Cu^{2+} and Ti^{4+} or Mg^{2+} and Ti^{4+}, and simultaneous substitution of Ni^{2+} and Mn^{4+} by Fe^{3+} were widely used to alleviate the structural degradation and increase the redox voltage.[16−20] However, these cathodes suffer from phase impurity when using the traditional solid-state sintering method and experience heterogeneous surface reconstruction, TM dissolution, and generation of intragranular cracks during repeated cycling.[21,22]

Recently, high-entropy materials, with multi-principal elements co-existing in a single phase, have gained significant attention due to their remarkable comprehensive performance. For example, high-entropy alloys have provided a substantial improvement of both strength and ductility,[23] and high-entropy oxides (HEO) achieve highly stable catalytic and electrochemical behavior.[24−26] When the high-entropy strategy was introduced in O3-type Na-ion layered oxide cathode by our group,[27] excellent cycling stability with delayed and highly reversible O3 to P3 transition has been demonstrated. However, equimolar mixtures of active and inactive TM caused slight capacity loss due to the reduction of redox couples. A similar situation was then found in a rocksalt-type high-entropy cation-disordered compound containing 12 TM species for the LIB cathode.[28] There can be a balance between high entropy and high capacity by adjusting the concentration of each TM. Additionally, the fundamental mechanisms of the impacts on structure−property relationship by high-entropy configuration are still not fully understood, especially the effect on capacity retention and thermal issue during prolonged cycling.

In this work, O3-$NaNi_{0.4}Fe_{0.2}Mn_{0.4}O_2$ (NFM424) was chosen as the baseline cathode material given the sufficient redox couples (such as Ni^{2+}/Ni^{4+} and Fe^{3+}/Fe^{4+}) and abundant Fe and Mn elements. We constructed high-entropy configuration in TMO_2 slabs of NFM424 by substituting divalent and tetravalent ions to form Na-$Ni_{0.25}Mg_{0.05}Cu_{0.1}Fe_{0.2}Mn_{0.2}Ti_{0.1}Sn_{0.1}O_2$ (HEO424), in which Cu^{2+} provides charge compensation, Mg^{2+} and Ti^{4+} stabilize the structural integrity, and Sn^{4+} helps to raise the average voltage, thus achieving a balance between the high entropy and TM redox couples. It is demonstrated that the pure O3-type phase is easily achieved in the high-entropy configuration oxide HEO424, where expanded TMO_2 slabs render fast Na^+ transport through an enlarged Na^+ octahedral−tetrahedral−octahedral transport channel and significantly alleviate the Jahn−Teller distortion of Ni^{3+}, Na^+/vacancy ordering, and lattice parameter changes. These structural features enable high-rate performance and keep structural integrity during long-term cycling with the suppression of TM dissolution and crack generation. Remarkably, we found that the thermal safety property of HEO424 is dramatically improved.

RESULTS AND DISCUSSION

Morphological and Structural Characterization. HEO424 and NFM424 were obtained by a high-temperature calcination process, as described in the Synthesis section in the Supporting Information. The overall compositions of the two comparable cathode materials were confirmed by inductively coupled plasma-atomic emission spectroscopy (ICP-AES), as shown in Table S1, and structural properties were analyzed by powder X-ray diffraction (XRD) and Rietveld refinement. Both cathode materials crystallize with an O3-type stacking sequence (Figure 1a), corresponding to the $NaFeO_2$ structure with an $R-3m$ symmetry. Rietveld refinement results (Tables S2 and S3) show that HEO424 adopts an alternative ordering of Na and TM occupation without any impurity phase, while the NFM424 has a minority of the NiO phase (3.5 wt %), which confirms that entropy regulates solid-solution formation as a result of the reduced Gibbs free energy according to $\Delta G = \Delta H - T\Delta S$.[29] Note that other multi-element compositions were synthesized as well but with different kinds of impurity phases as shown in Figure S1. Moreover, the lattice parameters of HEO424 (a = 3.0193 Å, c = 16.065 Å) increase significantly compared with those of NFM424 (a = 2.9661 Å, c = 15.989 Å). More specifically, the interlayer distances of $d_{(O-Na-O)}$ and $d_{(O-TM-O)}$ are calculated as 3.18 and 2.18 Å for HEO424, and 3.22 Å and 2.11 Å for NFM424, respectively. Although HEO424 shows a slightly smaller interlayer distance of NaO_2 slabs, the enlarged TMO_2 slabs permit the extension of intermediate triangular and tetrahedral space sites of the Na^+ transport channel (as illustrated in the schematic in Figure 1b), which is conducive to superior Na^+ transport kinetics. On the other hand, the ratio between the interlayer distances of $d_{(O-Na-O)}$ and $d_{(O-TM-O)}$ is calculated as 1.46, smaller than that of NFM424 (1.53), which implies the stability of O3 structure and delay of O3-P3 phase transition during Na^+ deintercalation, as stated in our previous work[9,30] and further demonstrated in the latter section. All the above results are attributed to the enlarged TMO_2 slabs originated from the variety of the ionic sizes and electronic properties, which especially weakens the electrostatic repulsion between the TMO_2 layers and expands the Na^+ transport channel.

The morphology of as-prepared cathode particles was characterized by scanning electron microscopy (SEM) and transmission electron microscopy (TEM). As depicted in Figure 1c and Figures S2 and S3, NFM424 shows a flake-like morphology with basal plane facets of approximately 2 μm wide and lateral facets of 300 nm thick, whereas HEO424 is elliptical ball-shaped with an average particle size of 2 μm. TEM images (Figure 1e,f) show that HEO424 and NFM424 have dense structures without any grain boundary, indicating that both samples exist as a single crystal. Furthermore, a high-angle annular dark-field (HAADF)-STEM image of a lay-flat NFM424 particle shows regular honeycomb TM arranged in hexagonal symmetry (viewed along the [001] crystallographic direction), which suggests that Na^+ transportation channels are distributed on the lateral surfaces, such as (100), (010), and (110), as indicated by the previous literature.[31,32] By contrast, the HEO424 cathode particles show the visualized Na^+ transportation channels perpendicular to the ellipsoidal surface, displaying more Na^+ storage space and thicker transportation layers (around 3 μm) than NFM424 (around 300 nm), as schematically illustrated in Figure 1d. HEO424, on the other hand, exhibiting a similar Na^+ transport distance but improved Na^+ storage space, will contribute to superior electrochemical performance and possibly bring higher tap density. The elaborate ellipsoidal morphology of HEO424 suggests that the high-entropy TMO_2 slabs significantly influence the crystal growth stage, especially the surface energy of the (003) lattice plane.[33]

https://doi.org/10.1021/jacs.2c02353
J. Am. Chem. Soc. XXXX, XXX, XXX−XXX

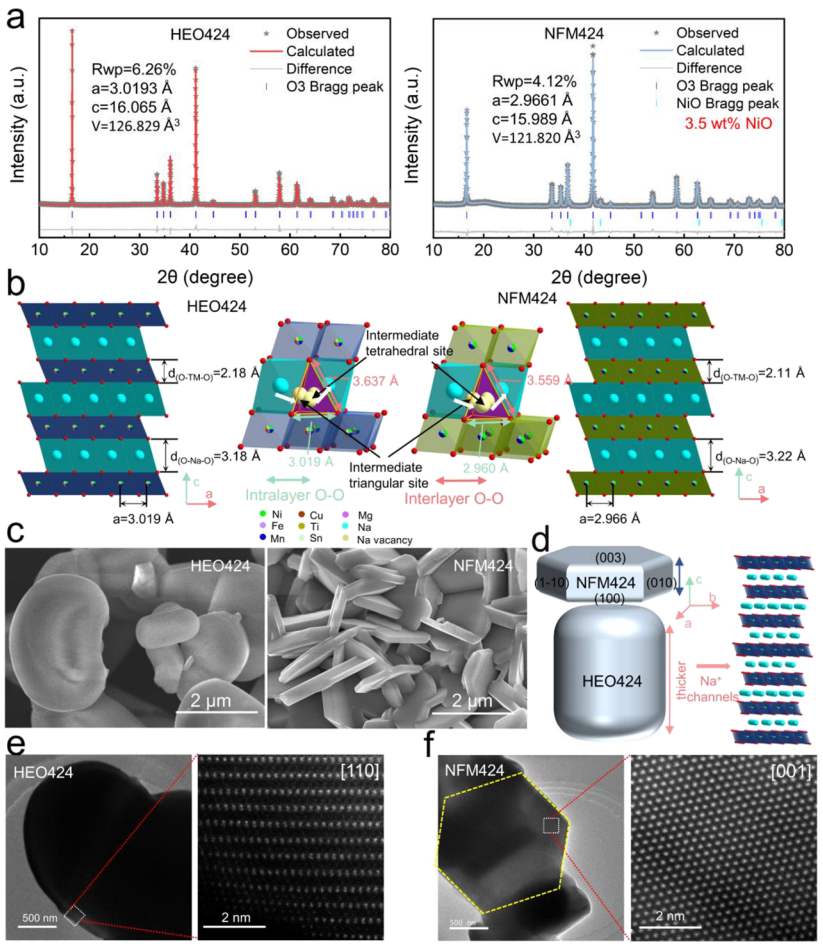

Figure 1. Characterization of structure and morphology of NFM424 and HEO424 cathodes. (a) XRD and Rietveld refinement patterns. (b) Schematic illustrations showing the Na^+ transport channels in both cathodes. (c) SEM images. (d) Schematic illustrations showing the morphological structure of both cathodes. TEM and HAADF-STEM images of HEO424 (e) and NFM424 (f).

Fundamental studies of crystal growth of inorganic compounds have shown that low surface energy planes in NFM424 exhibit much slower growth than that of the high surface energy planes, such as (100), (010), and (110) lattice planes, which tend to shrink or vanish during the growth. To unravel the modulation of surface energy by high-entropy configuration, the growth process of HEO424 was investigated by ex situ XRD and SEM techniques (Figures S4 and S5). XRD data indicate that O3 stacking dominates the whole phase formation of HEO424 and impurity phases gradually decrease (from Na_2SnO_3 + CuO + NiO to NiO then disappear) with the increase of calcination temperature. SEM images record the morphology evolution of HEO424, which first nucleated and grew into flake-like particles (average size 800 nm) as calcined at 800 °C and gradually grew to around 2 μm at 850 °C. A noticeable elliptical ball-shaped evolution is observed at 900 °C, but slight NiO nanoparticles are attached to the particle surface. Further increasing the sintering temperature to 950 °C, all TMs were completely dissolved into the lattice, forming elliptical ball-shaped particles with a high-entropy configuration O3 phase. The above results confirm that the thin, flake-like particles are gradually transformed into large elliptical balls through entropy increase in TMO_2 slabs with the increase of sintering temperature. A possible reason is that the high-entropy configuration in TMO_2 slabs significantly improves the surface energy of the (003) lattice plane, leading to the isotropic growth of cathode particles. More importantly, this further indicates that a high-entropy configuration design can effectively enhance the structural stability of the O3 structure through the enhanced TM−O and Na−O bonding energy, which can also contribute to the robust lattice skeleton for Na^+ (de)intercalation. Elemental mapping analysis by means of STEM-energy dispersive X-ray spectroscopy (EDS) shows that both NFM424 and HEO424 cathodes are compositionally homogeneous without detectable elemental segregation at a single particle (Figures S6 and S7).

Electrochemical Performance. Given the refined structure variation of the as-prepared cathodes, it was of great significance to investigate correlations between the electrochemical property and the high-entropy configuration design. The Na^+ storage performance of the HEO424 and the NFM424 cathodes was first explored by using coin-type half cells with a Na metal anode. As shown in Figure 2a,b, the HEO424 cathode delivers a reversible capacity of 130.8 mAh g^{-1} in the voltage range of 2.0−4.0 V at 0.1C (14 mA g^{-1}), slightly less than that of 135.6 mAh g^{-1} for the NFM424 counterpart because HEO424 has a much higher molar mass and fewer redox couples. Even so, both cathodes have a reversible Na^+ intercalation amount of 0.57 mol, which highlights the importance of the more open Na^+ diffusion channel in HEO424 material. The reversible capacity is much

https://doi.org/10.1021/jacs.2c02353
J. Am. Chem. Soc. XXXX, XXX, XXX−XXX

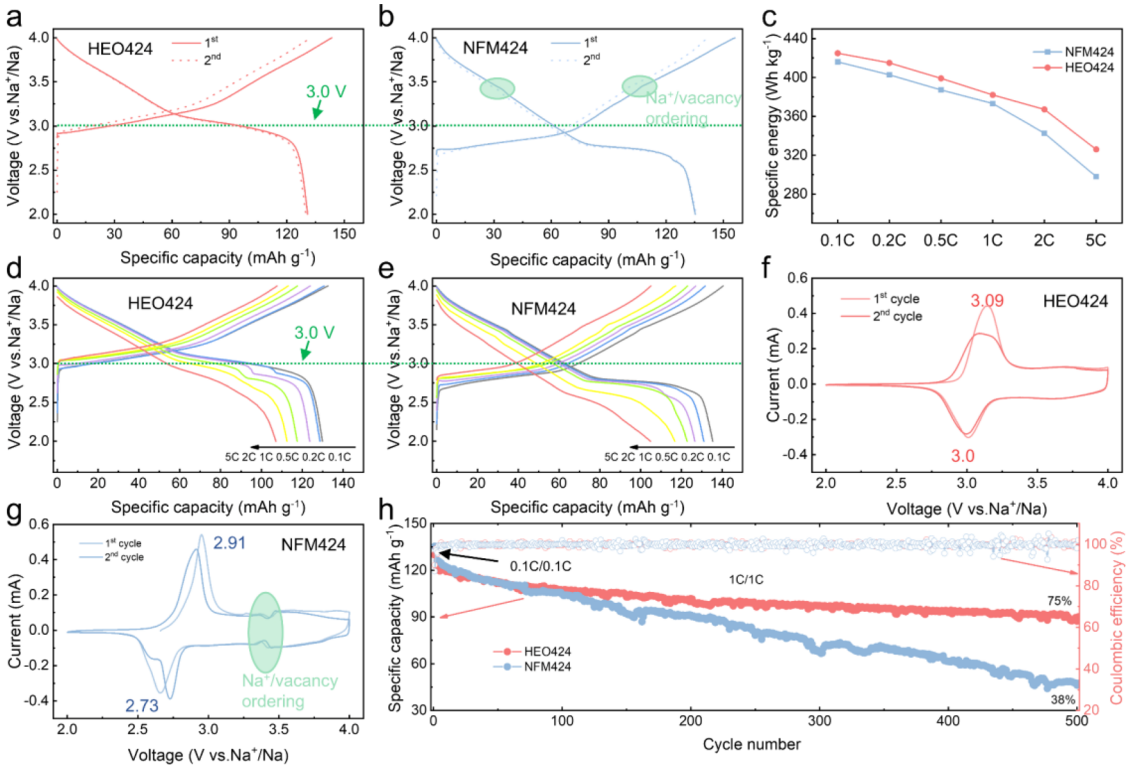

Figure 2. Electrochemical performances of HEO424 and NFM424 cathodes. Initial charge−discharge curves of HEO424 (a) and NFM424 (b) cathodes at 0.1 C during cycling between 2.0 and 4.0 V (vs Na^+/Na). (c) Energy density of both cathode materials when cycled at 0.1, 0.2, 0.5, 1.0, 2.0, and 5.0 C. Charge−discharge curves of HEO424 (d) and NFM424 (e) cathodes during rate tests. CV profiles of the HEO424 (f) and NFM424 (g) electrodes in the first and second cycles at 0.1 mV s^{-1}. (h) Cycling performance of both cathodes at 1.0 C.

higher than that of our previously reported HEO cathode (~110 mAh g^{-1}).[27] Similarly, the rate capacities of HEO424 are slightly less than that of the NFM424 cathode, as shown in Figure S8, until reaching 5C, the capacities of the HEO424 cathode outperform that of the NFM424 cathode (108 vs 104 mAh g^{-1}, corresponding to 82.5 and 76.5% of their initial capacity, respectively). However, the energy density of HEO424 is much higher than that of the NFM424 cathode among all the current rates (Figure 2c), such as 421 vs 414 Wh Kg^{-1} at 0.1C, which originates from the higher average voltage (Figure 2d,e) benefiting from the element substitution with the increase of TM−O bond ionicity.[19] The high energy density would significantly promote the practical application of layered oxide cathodes for NIBs. The initial Coulombic efficiencies for HEO424 and NFM424 were 91 and 87%, respectively, indicating less parasitic reactions and irreversible capacity loss for HEO424.

As shown in the cyclic voltammetry (CV) profiles obtained from both cathodes (Figure 2f,g), much more symmetrical anodic/cathodic peaks at higher voltage (3.09/3.0 V) can be clearly observed for the HEO424 cathode, consistent with the galvanostatic profiles. Moreover, the NFM424 shows additional anodic and cathodic peaks at 3.4−3.5 V, which is attributed to the Na^+/vacancies order−disorder transition.[7] However, no such peaks are seen for the HEO424 cathode. In this case, the high-entropy configuration in HEO424 might reduce the ordering of Na^+/vacancies upon Na^+ (de)-intercalation. This is because multicomponent distribution in TM layers provides uniform charge distribution, thus contributing to the rapid and reversible Na^+ (de)intercalation. Figure 2h shows the capacity retentions at 1C/1C charge−discharge over 500 cycles. When operated within a voltage range of 2.0−4.0 V, NFM424 shows serious capacity degradation (from the initial capacity of 126 mAh g^{-1} to 47.4 mAh g^{-1}), consistent with the previous report.[34] By contrast, HEO424 displays much improved capacity retention with a capacity of 90 mAh g^{-1}(75% of the initial capacity), demonstrating the significantly enhanced skeleton structure of HEO424. To gain a deeper understanding of the improved electrochemical property, galvanostatic intermittent titration technique (GITT) measurements were conducted to explore the Na^+ transportation kinetics in both cathodes (Figure S9). Apparent Na^+ diffusion coefficients were calculated from the GITT and divided by the different phase regions. The NFM424 maintains Na^+ diffusion coefficients of 2×10^{-11} to 6×10^{-11} cm^2 s^{-1} at the plateau and slope area of the initial charge−discharge curves, which usually corresponds to O3-type and P3-type structures. Whereas, the apparent Na^+ diffusion coefficients of HEO424 are twice higher than that of NFM424 in both regions, indicating that HEO424 has improved Na^+ kinetics. The improved Na^+ kinetics of HEO424 is further supported by cyclic voltammetry results (Figure S10). Based on the above results, it is confirmed that high-entropy configuration in the layered oxide cathode notably improves their electrochemical performances.

Alleviated Structural Evolution. To assess the influence of high-entropy configuration on the electrochemical reaction of the layered oxide cathode, in situ XRD measurements were carried out on the NFM424 and HEO424 electrodes during charging to 4.0 V at 0.1C. Figure 3 shows the first charge curves and the two-dimensional (2D) contour plots of the main diffraction peak evolution for NFM424 and HEO424.

https://doi.org/10.1021/jacs.2c02353
J. Am. Chem. Soc. XXXX, XXX, XXX−XXX

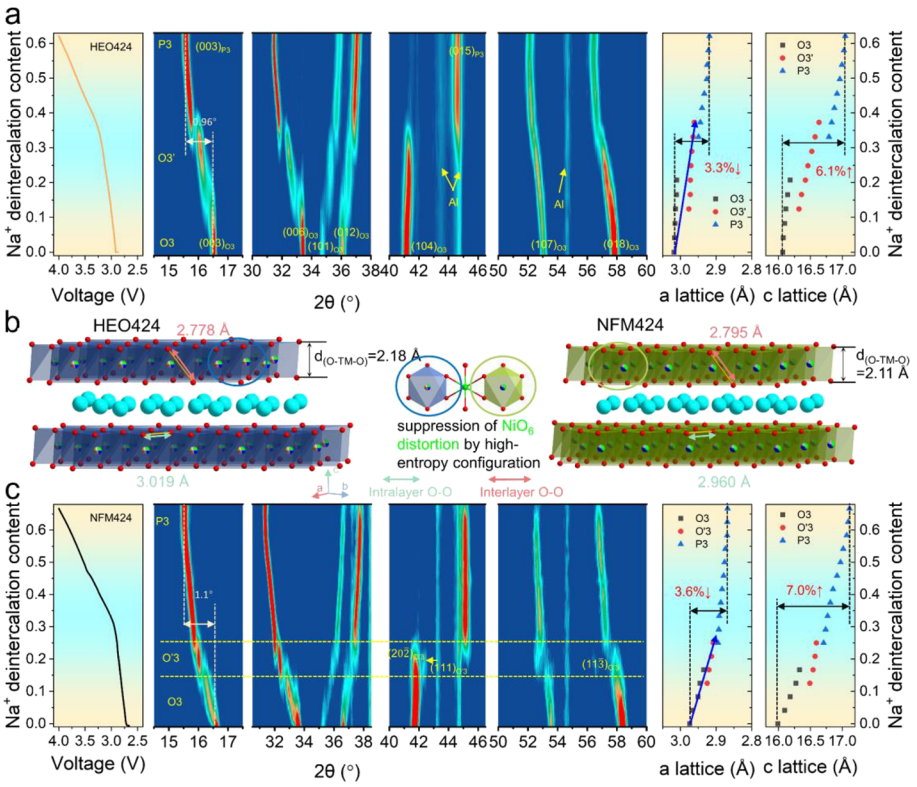

Figure 3. Structural evolution during the initial charge process. 2D contour plots of in situ XRD during the structural evolution of HEO424 (a) and NFM424 (c) cathodes. (b) Schematic illustrations showing the TMO_2 slabs in both cathodes. The first charge curves as a function of Na^+ deintercalation content are plotted on the right, and the *a*/*c*-axis lattice parameter changes in the as-prepared samples obtained by fitting the in situ XRD data are plotted on the left.

Even though the (003) peaks of both electrodes shift initially to a lower angle and gradually split into two peaks, suggesting *c*-axis expansion accompanied by a phase transition, the phase transitions of the two cathodes are quite different. The formation of an intermediate O′3 phase (monoclinic, C2/m) in NFM424 is implied by the splitting of the (104) peak into (20−2) and (111). This O′3 phase is formed by the collective Jahn−Teller distortion caused by the increasing amount of Ni^{3+} upon Na^+ deintercalation. However, the intensity and position of the (104) peaks for the HEO424 change smoothly, and no new peak appears during the initial charge process, suggesting that the hexagonal to monoclinic phase transition has been successfully suppressed, and only a Na-deficient O3' phase (hexagonal similar to the pristine O3 structure) is formed, consistent with our previous report.[27] The absence of the O′3 structure during the phase transitions can be explained by the lack of long-range Na^+/vacancy ordering and concentrated Jahn−Teller distortion as a result of multi-component TM layers, which reduce and disrupt the Ni^{3+} ordering. Moreover, enlarged TMO_2 slabs (Figure 3b) might relieve Jahn−Teller distortion of the Ni^{3+} active center and have a strong tendency to high-symmetric structures, consistent with the recent literature.[35] During the further charging process, both electrodes experience a phase evolution to the P3 phase, which is accompanied by the gliding of TM layers, and maintain the P3 phase until the end of charge. It is worth noting that the P3 phase appears upon approximately 0.25 and 0.33 mol Na^+ being deintercalated out of the host structure for NFM424 and HEO424, respectively, indicating the delay of O3-P3 phase transition in HEO424 cathode upon charging. We further introduced the cationic potential (Φ_{cation}) to qualitatively investigate the favorable stacking structures upon Na^+ deintercalation, and the computational detail is presented in Table S4. As shown in Figure S11, HEO424 shows a smaller cationic potential than NFM424 regardless of the pristine state or Na-deficient state (0.33 mole of Na^+ deintercalation), and further away from the line, separating the P- and O-type phases, this demonstrates that HEO424 maintains the O3 structure more steadily and endurably at the early Na^+ deintercalation process, agreeing well with the above XRD refinement results.

In typical alkali-ion layered oxide cathodes, strong anisotropic evolution of the crystal structure during alkali-ion (de)intercalation usually causes chemo-mechanical cracking; particularly, the lattice expansion and contraction of Na-ion layered oxide cathodes are more serious than that in Li counterparts due to the larger size of Na^+ and the stronger repulsion of Na^+−Na^+. Lattice parameter evolutions are examined in response to internal stress inside particles, which can be directly tracked by in situ XRD measurements. As shown in Figure 3, HEO424 and NFM424 undergo different lattice expansions and contractions along the *c*-axis and *a*-axis in the charging process. Even though the actual Na^+ extraction amounts and the oxidation state changes of transition metals in NFM424 and HEO424 are very close, lattice parameter changes along the *a*-axis are less in HEO424, suggesting that the high-entropy configuration of TM layers can accommodate a greater extent size changes of transition metal ions. In particular, the HEO424 shows slighter lattice contraction along the *a*-axis in the initial Na^+ extraction process compared to NFM424 (as indicated by blue arrows in the right of Figure 3), which demonstrates that enlarged

https://doi.org/10.1021/jacs.2c02353
J. Am. Chem. Soc. XXXX, XXX, XXX−XXX

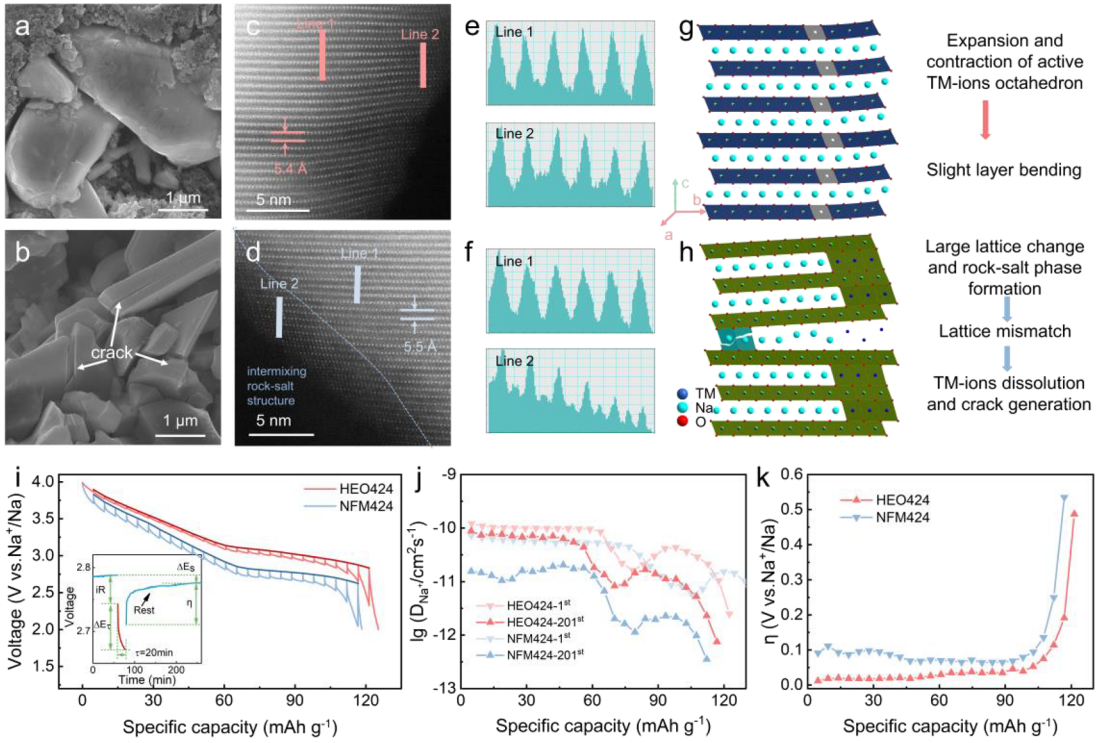

Figure 4. Morphological and microstructural evolution and Na^+ storage kinetics of HEO424 and NFM424 cathodes after 200 cycles. SEM and HAADF-STEM images of the HEO424 (a, c) and NFM424 (b, d) cathodes after 200 cycles. (e, f) Intensity profile corresponding to line 1 and line 2 in (c) and (d), respectively. Schematic illustration of the structural evolution of HEO424 (g) and NFM424 (h) cathodes after 200 cycles. (i) GITT curves (light color) and their open-circuit voltage (OCV) curves (dark color) of HEO424 and NFM424 in the 201st discharge cycle; the inset is the representative titration process. (j) Na^+ diffusivity calculated from (i) and the first cycles in Figure S9. (k) overpotential (η) at different states of discharge obtained from (i).

TMO_2 slabs will relieve Jahn−Teller distortion of the Ni^{3+}. Moreover, the increase of the *c*-lattice parameter induced by the electrostatic repulsion of adjacent oxygen layers in the NaO_2 slabs is less pronounced, indicating that the HEO424 layered framework structure has a smaller local interaction between Na^+ in NaO_2 slabs.[27] In contrast, the NFM424 layered framework structure with an intense local interaction further confirms the occurrence of Na^+/vacancies order−disorder transition during the repeated charge/discharge process, indicating inferior Na^+ diffusivity. In addition, the strains and mechanical degradation of this material would be serious during long-term cycling. Therefore, the enhanced electrochemical properties of the HEO424 can be explained by the fewer phase transitions (including the Na^+/vacancies order−disorder transition) and the weaker anisotropy of the mechanical properties, which lead to lower structural distortion and reduced mechanical degradation of the cathode. During the discharging and second charging process, the HEO424 cathode displays a highly reversible O3-P3 phase evolution behavior, as shown in Figure S12, which is likely to spur further improvements in long-term cycling performance.

Effects on Structural Integrity and Stability. We further characterized the morphological and microstructural evolution of NFM424 and HEO424 cathodes after cycling at the grain-level and atomic-scale by means of SEM and HAADF-STEM to unravel the extraordinary effect of high-entropy configuration. After 200 cycles under a 1C/1C charge/discharge rate, various tiny cracks appeared in NFM424 particles but none appeared for the HEO424 particles, which still kept a robust single crystal morphology as shown by SEM (Figure 4a,b). This notably different behavior further verifies that the stress evolution in the HEO424 cathode along with phase transitions during cycling is effectively mitigated. In addition, from the atomic-resolution STEM images (Figure 4c,d), a severe Na^+/TM intermixing rock-salt structure ($Fd3m$) is observed on the surface, epitaxially growing on the edges of the NFM424 particles along the (003) plane, up to several nanometers in length. In contrast, there was only a slight curvature of the TMO_2 slabs near the surface for HEO424 particles without a trace of the rock-salt phase. Furthermore, the line profile intensity of HAADF-STEM images shown in Figure 4e,f, demonstrates that NFM424 possesses an obvious rock-salt phase in its near-surface region but a layered phase in its interior, while HEO424 exhibits a layered phase in both the surface and interior. Although the surface rock-salt phase only occupies a very slight proportion compared with the substantial bulk phase of a single grain, such surface reconstruction in the NFM424 cathode plays the crucial role in determining the layered oxide cathodes' electrochemical stability during long-term cycling because that surface structure serves as the gate to regulate the (de)intercalation of Na^+ from or into the electrolyte. Additionally, there is a serious lattice and ion space size mismatch between the surface inactive rock-salt phase and layered bulk phase, especially during the Na^+ (de)intercalation process,[36] which can result in a serious TM dissolution and spontaneous material fatigue, thus leading to prominent capacity decay of the NFM424 cathode. The much severe dissolution of TM in the NFM424 cathode was further demonstrated via ICP-AES and digital photographs of the separators, as shown in Table S5 and Figure S13. Figure 4g,h

https://doi.org/10.1021/jacs.2c02353
J. Am. Chem. Soc. XXXX, XXX, XXX−XXX

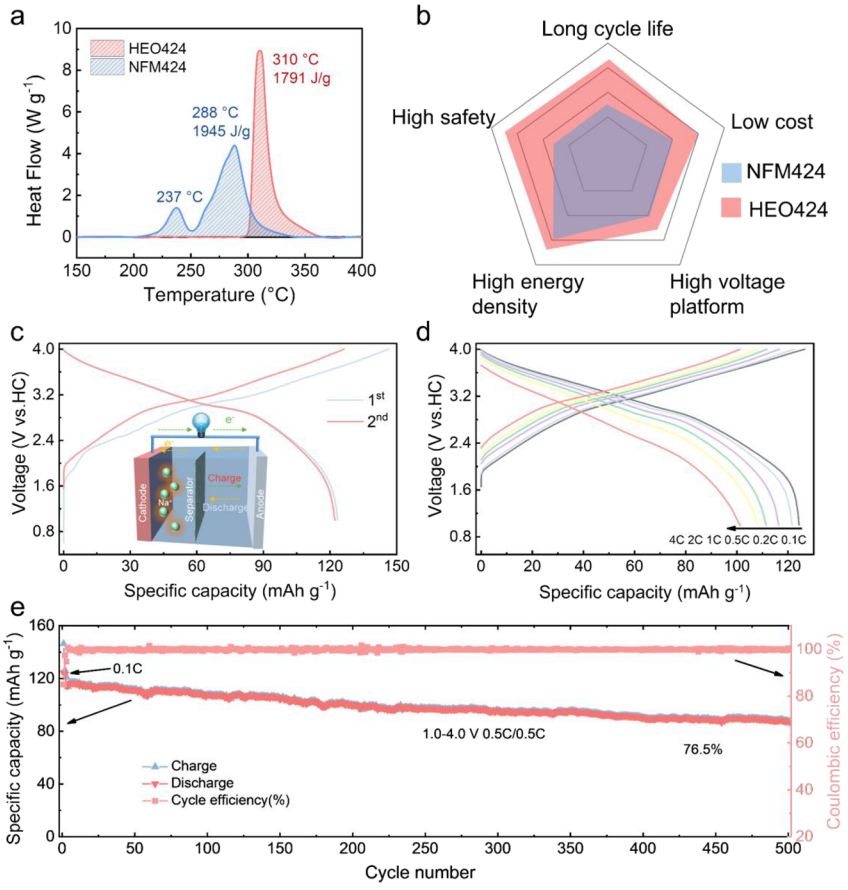

Figure 5. (a) DSC profiles of NFM424 and HEO424 cathode materials charged to 4.0 V with a heating rate of 5 °C min^{-1}. (b) Radar maps of the NIBs based on these two cathode materials. (c) Initial charge−discharge curves of the full cell of HEO424 cathode and hard carbon anode in the range of 1.0−4.0 V at 0.1C, inset is a schematic drawing of the full-cell configuration. (d) Charge−discharge voltage of the full cell at various rates. (e) Cycling performance of the full-cell at 0.5 C.

illustrates the different structural evolution behaviors of the HEO424 and NFM424 particles. For the HEO424 sample, contraction and expansion of the active TMO_6 octahedron during charge/discharge only lead to the slight bending of TMO_2 slabs, which have been well protected by the robust TMO_2 slabs, thereby contributing to its superior electrochemical property. In contrast, large lattice parameter changes resulting from fatigued TMO_2 slabs and rock-salt phase formation caused by TM migration will generate a prominent lattice mismatch in the NFM424 sample. Therefore, the intensive strain between layered O3 or P3 structures with larger spacing and the rock-salt structure with smaller spacing is promoted to induce considerable TM dissolution and crack generation, which well explains the inferior electrochemical performance.

GITT measurements were further conducted to probe the Na^+ diffusion kinetics in both cathodes after 200 cycles. As reported in the previous literature, Ohmic resistance and Na^+ diffusion limitation are part of kinetic polarization, which can be decoupled from other limitation factors (such as structural integrity) by using a low current rate or investigated more elaborately by the GITT test.[37,38] As shown in Figure 4i, according to the 201st discharge measured by GITT at a current density of 14 mA g^{-1}, HEO424 exhibited a much stronger ability to recover from long-term cycling than NFM424. After 200 cycles at 1C/1C charge/discharge, the HEO424 can release 96% of the initial reversible capacity (at a low current rate) compared with that of 87% for NFM424, which results from the crack generation and TM dissolution. Such structural deterioration would lead to the loss of active Na^+ storage sites and a redox-active center, which is consistent with the STEM observation displayed above. Furthermore, the Na^+ diffusivities (D_{Na+}) in both cathodes were calculated from GITT and compared in Figure 4j. It is distinct that the average D_{Na+} in HEO424 was almost one order of magnitude higher than that of NFM424 in the 201st cycle and nearly close to the value of 1.2×10^{-10} cm^2 s^{-1} during the first discharge, undoubtedly due to the robust layered lattices in HEO424. In addition, the cumulated overpotential (η) and IR drop (Figure 4k and Figure S14) were significantly mitigated compared to that of NFM424, indicating that the suppressed TM dissolution from the HEO cathode successfully alleviates their dissolution in the electrolyte or deposition at the anode, greatly improving the stability of the SEI and interfacial Na^+ transfer.[39,40] These results demonstrate that the well-maintained layered phase by high-entropy configuration in TMO_2 slabs helps improve the thermodynamic stability and electrochemical dynamics of the whole battery in cycling.

Evaluation of High-Entropy Configuration toward Practical Applications. The thermal stability of electrode materials under high voltage charging is another crucial indicator for the practical applications of NIBs, which is related to the safety requirements of NIBs.[41] Differential scanning calorimetry (DSC) as an efficient thermal analysis

https://doi.org/10.1021/jacs.2c02353
J. Am. Chem. Soc. XXXX, XXX, XXX−XXX

technique was used to detect the thermal effect of high-entropy configuration in TMO_2 slabs. For a direct comparison, both electrodes were evaluated at the charged state of 4.0 V (with a similar Na^+ deintercalation amount) and with the presence of an electrolyte (1 M $NaPF_6$ in EC/PC with 2% FEC, electrolyte-to-cathode mass ratio of 2:1). As shown in Figure 5a, the obvious exothermic peaks can be indexed to oxygen release from the crystal structure and reduction of active TM upon heating, which leads to the phase transition of the P3 phase to the TM_3O_4 structure (space group: $Fd3m$) accompanied by the heat generation.[42,43] The NFM424 cathode displays exothermal peaks at around 237 and 288 °C with a heat generation of 1945 $J{\cdot}g^{-1}$, whereas the HEO424 cathode displays exothermal peaks at a significantly higher temperature (310 °C) and the overall heat generation was reduced to 1791 $J{\cdot}g^{-1}$. The oxygen release for the charged dry electrodes was also confirmed by thermogravimetric analysis (TGA), which shows much more weight losses at the earlier stage in the NFM424 electrode associated with the oxygen release (Figure S15). Note that repeated DSC and TGA tests of each electrode were conducted at least three times to maintain consistency. Therefore, these results demonstrate that the multicomponent distribution in TMO_2 slabs of layered oxides can suppress oxygen release and thermal runaway stems from the enhanced TM-O bonding energy, thus maintaining the structural integrity and improving thermal safety.

Overall, we obtained a comparative analysis of these two electrodes' electrochemical performances based on the material level (half-cell), as illustrated in Figure 5b, including cycle life, cost, voltage platform, energy density, and safety. The HEO424 material exhibits improved capability in all aspects compared to the NFM424 counterpart and can adapt to the different demands of energy storage and power batteries, including high energy density, long cycle life, low cost, and high safety. Furthermore, with the same gravimetric energy density, the elevated average operating voltage will efficiently reduce the consumption of the negative electrode, thus further enhancing the volumetric energy density.

For potential practical applications, coin-type full cells with the HEO424 cathode and hard carbon (HC) anode were assembled and cycled in the voltage range of 1.0−4.0 V. The full cell has an initial Coulombic efficiency of 84.4% with a reversible specific capacity of 123.5 mAh g^{-1} (based on cathode mass) and energy density of 260 Wh kg^{-1} (based on the total mass of active materials) at 0.1C (Figure 5c), which outperformed most conventional layered oxide cathodes.[44,45] To verify the high-power characteristic of this full cell, various charge−discharge rates were applied. As shown in Figure 5d and Figure S16, when the discharge current rates increase from 0.1 to 4 C, the full cell has a capacity retention of 81%. After the rate cycling test, a reversible capacity of ∼123 mAh g^{-1} is still obtained at 0.1 C, suggesting excellent reversibility. The long-term cycle performance of the HEO424 full cell was carried out at 0.5 C charge−discharge. As shown in Figure 5e, the full cell remains 76.5% of the initial capacity after 500 cycles with a Coulombic efficiency above 99.6%, which we believe will be further improved with electrolyte optimization. Therefore, the excellent electrochemical performance and thermal stability will promote the application of the HEO424 cathode in NIBs for stationary energy storage systems with a high performance to price ratio and superior safety.

CONCLUSIONS

In summary, gathered evidences show that high-entropy configuration TMO_2 slabs in a single-phase O3-$Na[Ni_{0.25}Mg_{0.05}Cu_{0.1}Fe_{0.2}Mn_{0.2}Ti_{0.1}Sn_{0.1}]O_2$ can readily help boost morphological and structural improvement to achieve large Na^+ storage space and delayed phase transition, leading to exceptional rate and cycle performances without energy density trade-off. Due to the strengthened TMO_2 skeleton, severe TM dissolution and cracking generation observed in NFM424 are suppressed for HEO424 cathode particles. Moreover, improved thermal stability in HEO424 has also been revealed. Therefore, we believe that this high-entropy configuration design in TMO_2 slabs of the layered oxide cathodes has demonstrated the important role of the TMO_2 skeleton in the cation redox and Na^+ (de)intercalation process, which would contribute to curing the structural instability of layered oxide cathodes (especially the Na/K-ion layered oxides) and thereby facilitating their implementation in practical applications.

ASSOCIATED CONTENT

Supporting Information

The Supporting Information is available free of charge at https://pubs.acs.org/doi/10.1021/jacs.2c02353.

Experimental details, additional electrochemical, SEM and XRD characterization results, and details of plots of additional figures and tables (PDF)

AUTHOR INFORMATION

Corresponding Authors

Xiaohui Rong − *Key Laboratory for Renewable Energy, Beijing Key Laboratory for New Energy Materials and Devices, Beijing National Laboratory for Condensed Matter Physics, Institute of Physics, Chinese Academy of Sciences, Beijing 100190, China; College of Materials Science and Optoelectronic Technology, University of Chinese Academy of Sciences, Beijing 100049, China; Huairou Division, Institute of Physics, Chinese Academy of Sciences, Beijing 101400, China*; Email: rong@iphy.ac.cn

Yaxiang Lu − *Key Laboratory for Renewable Energy, Beijing Key Laboratory for New Energy Materials and Devices, Beijing National Laboratory for Condensed Matter Physics, Institute of Physics, Chinese Academy of Sciences, Beijing 100190, China; Huairou Division, Institute of Physics, Chinese Academy of Sciences, Beijing 101400, China; Yangtze River Delta Physics Research Center Co. Ltd., Liyang 213300, China*; orcid.org/0000-0001-5202-175X; Email: yxlu@iphy.ac.cn

Yong-Sheng Hu − *Key Laboratory for Renewable Energy, Beijing Key Laboratory for New Energy Materials and Devices, Beijing National Laboratory for Condensed Matter Physics, Institute of Physics, Chinese Academy of Sciences, Beijing 100190, China; College of Materials Science and Optoelectronic Technology, University of Chinese Academy of Sciences, Beijing 100049, China; Huairou Division, Institute of Physics, Chinese Academy of Sciences, Beijing 101400, China; Yangtze River Delta Physics Research Center Co. Ltd., Liyang 213300, China*; orcid.org/0000-0002-8430-6474; Email: yshu@iphy.ac.cn

https://doi.org/10.1021/jacs.2c02353
J. Am. Chem. Soc. XXXX, XXX, XXX−XXX

Authors

Feixiang Ding − *Key Laboratory for Renewable Energy, Beijing Key Laboratory for New Energy Materials and Devices, Beijing National Laboratory for Condensed Matter Physics, Institute of Physics, Chinese Academy of Sciences, Beijing 100190, China; Huairou Division, Institute of Physics, Chinese Academy of Sciences, Beijing 101400, China;* orcid.org/0000-0002-4028-6141

Chenglong Zhao − *Key Laboratory for Renewable Energy, Beijing Key Laboratory for New Energy Materials and Devices, Beijing National Laboratory for Condensed Matter Physics, Institute of Physics, Chinese Academy of Sciences, Beijing 100190, China*

Dongdong Xiao − *Key Laboratory for Renewable Energy, Beijing Key Laboratory for New Energy Materials and Devices, Beijing National Laboratory for Condensed Matter Physics, Institute of Physics, Chinese Academy of Sciences, Beijing 100190, China*

Haibo Wang − *Key Laboratory for Renewable Energy, Beijing Key Laboratory for New Energy Materials and Devices, Beijing National Laboratory for Condensed Matter Physics, Institute of Physics, Chinese Academy of Sciences, Beijing 100190, China*

Yuqi Li − *Key Laboratory for Renewable Energy, Beijing Key Laboratory for New Energy Materials and Devices, Beijing National Laboratory for Condensed Matter Physics, Institute of Physics, Chinese Academy of Sciences, Beijing 100190, China; College of Materials Science and Optoelectronic Technology, University of Chinese Academy of Sciences, Beijing 100049, China;* orcid.org/0000-0003-1501-1549

Yang Yang − *Key Laboratory for Renewable Energy, Beijing Key Laboratory for New Energy Materials and Devices, Beijing National Laboratory for Condensed Matter Physics, Institute of Physics, Chinese Academy of Sciences, Beijing 100190, China; College of Materials Science and Optoelectronic Technology, University of Chinese Academy of Sciences, Beijing 100049, China*

Complete contact information is available at: https://pubs.acs.org/10.1021/jacs.2c02353

Notes

The authors declare no competing financial interest.

■ ACKNOWLEDGMENTS

This work was supported by the Strategic Priority Research Program of the Chinese Academy of Sciences (XDA21070500), the National Natural Science Foundation (NSFC) of China (51725206, 52122214 and 52072403), Youth Innovation Promotion Association of the Chinese Academy of Sciences (2020006), China Postdoctoral Science Foundation founded Project (2021M703460), and Beijing Municipal Natural Science Foundation (2212022).

■ REFERENCES

(1) Hu, Y.-S.; Li, Y. Unlocking Sustainable Na-Ion Batteries into Industry. *ACS Energy Lett.* **2021**, *6*, 4115−4117.

(2) Hwang, J. Y.; Myung, S. T.; Sun, Y. K. Sodium-ion batteries: present and future. *Chem. Soc. Rev.* **2017**, *46*, 3529−3614.

(3) Rong, X.; Hu, E.; Lu, Y.; Meng, F.; Zhao, C.; Wang, X.; Zhang, Q.; Yu, X.; Gu, L.; Hu, Y.-S.; Li, H.; Huang, X.; Yang, X.-Q.; Delmas, C.; Chen, L. Anionic Redox Reaction-Induced High-Capacity and Low-Strain Cathode with Suppressed Phase Transition. *Joule* **2019**, *3*, 503−517.

(4) Berthelot, R.; Carlier, D.; Delmas, C. Electrochemical investigation of the P2-Na_xCoO_2 phase diagram. *Nat. Mater.* **2011**, *10*, 74−80.

(5) Ding, F.; Zhao, C.; Zhou, D.; Meng, Q.; Xiao, D.; Zhang, Q.; Niu, Y.; Li, Y.; Rong, X.; Lu, Y.; Chen, L.; Hu, Y.-S. A Novel Ni-rich O3-$Na[Ni_{0.60}Fe_{0.25}Mn_{0.15}]O_2$ Cathode for Na-ion Batteries. *Energy Storage Mater.* **2020**, *30*, 420−430.

(6) Yabuuchi, N.; Kajiyama, M.; Iwatate, J.; Nishikawa, H.; Hitomi, S.; Okuyama, R.; Usui, R.; Yamada, Y.; Komaba, S. P2-type $Na_x[Fe_{1/2}Mn_{1/2}]O_2$ made from earth-abundant elements for rechargeable Na batteries. *Nat. Mater.* **2012**, *11*, 512−517.

(7) Komaba, S.; Yabuuchi, N.; Nakayama, T.; Ogata, A.; Ishikawa, T.; Nakai, I. Study on the reversible electrode reaction of $Na_{1-x}Ni_{0.5}Mn_{0.5}O_2$ for a rechargeable sodium-ion battery. *Inorg. Chem.* **2012**, *51*, 6211−6220.

(8) Somerville, J. W.; Sobkowiak, A.; Tapia-Ruiz, N.; Billaud, J.; Lozano, J. G.; House, R. A.; Gallington, L. C.; Ericsson, T.; Häggström, L.; Roberts, M. R.; Maitra, U.; Bruce, P. G. Nature of the "Z"-phase in layered Na-ion battery cathodes. *Energy Environ. Sci.* **2019**, *12*, 2223−2232.

(9) Zhao, C.; Yao, Z.; Wang, Q.; Li, H.; Wang, J.; Liu, M.; Ganapathy, S.; Lu, Y.; Cabana, J.; Li, B.; Bai, X.; Aspuru-Guzik, A.; Wagemaker, M.; Chen, L.; Hu, Y. S. Revealing High Na-Content P2-Type Layered Oxides as Advanced Sodium-Ion Cathodes. *J. Am. Chem. Soc.* **2020**, *142*, 5742−5750.

(10) Wang, Y.; Xiao, R.; Hu, Y. S.; Avdeev, M.; Chen, L. P2-$Na_{0.6}[Cr_{0.6}Ti_{0.4}]O_2$ cation-disordered electrode for high-rate symmetric rechargeable sodium-ion batteries. *Nat. Commun.* **2015**, *6*, 6954.

(11) Wang, P. F.; Yao, H. R.; Liu, X. Y.; Yin, Y. X.; Zhang, J. N.; Wen, Y.; Yu, X.; Gu, L.; Guo, Y. G. Na^+/vacancy disordering promises high-rate Na-ion batteries. *Sci. Adv.* **2018**, *4*, eaar6018.

(12) Komaba, S.; Takei, C.; Nakayama, T.; Ogata, A.; Yabuuchi, N. Electrochemical intercalation activity of layered $NaCrO_2$ vs. $LiCrO_2$. *Electrochem. Commun.* **2010**, *12*, 355−358.

(13) Kikkawa, S.; Miyazaki, S.; Koizumi, M. Sodium deintercalation from α-$NaFeO_2$. *Mater. Res. Bull.* **1985**, *20*, 373−377.

(14) Miyazaki, S.; Kikkawa, S.; Koizumi, M. Chemical and electrochemical deintercalations of the layered compounds $LiMO_2$ (M = Cr, Co) and $NaM'O_2$ (M′ Cr, Fe, Co, Ni). *Synth. Met.* **1983**, *6*, 211−217.

(15) Braconnier, J. J.; Delmas, C.; Hagenmuller, P. Etude par desintercalation electrochimique des systemes Na_xCrO_2 et Na_xNiO_2. *Mater. Res. Bull.* **1982**, *17*, 993−1000.

(16) Kubota, K.; Fujitani, N.; Yoda, Y.; Kuroki, K.; Tokita, Y.; Komaba, S. Impact of Mg and Ti doping in O3 type $NaNi_{1/2}Mn_{1/2}O_2$ on reversibility and phase transition during electrochemical Na intercalation. *J. Mater. Chem. A* **2021**, *9*, 12830−12844.

(17) Yao, H. R.; Wang, P. F.; Gong, Y.; Zhang, J.; Yu, X.; Gu, L.; OuYang, C.; Yin, Y. X.; Hu, E.; Yang, X. Q.; Stavitski, E.; Guo, Y. G.; Wan, L. J. Designing Air-Stable O3-Type Cathode Materials by Combined Structure Modulation for Na-Ion Batteries. *J. Am. Chem. Soc.* **2017**, *139*, 8440−8443.

(18) Wang, Q.; Mariyappan, S.; Vergnet, J.; Abakumov, A. M.; Rousse, G.; Rabuel, F.; Chakir, M.; Tarascon, J. M. Reaching the Energy Density Limit of Layered O3-$NaNi_{0.5}Mn_{0.5}O_2$ Electrodes via Dual Cu and Ti Substitution. *Adv. Energy Mater.* **2019**, *9*, 1901785.

(19) Sathiya, M.; Jacquet, Q.; Doublet, M.-L.; Karakulina, O. M.; Hadermann, J.; Tarascon, J.-M. A Chemical Approach to Raise Cell Voltage and Suppress Phase Transition in O3 Sodium Layered Oxide Electrodes. *Adv. Energy Mater.* **2018**, *8*, 1801975.

(20) Wang, P. F.; Yao, H. R.; Liu, X. Y.; Zhang, J. N.; Gu, L.; Yu, X. Q.; Yin, Y. X.; Guo, Y. G. Ti-Substituted $NaNi_{0.5}Mn_{0.5-x}Ti_xO_2$ Cathodes with Reversible O3-P3 Phase Transition for High-Performance Sodium-Ion Batteries. *Adv. Mater.* **2017**, *29*, 1700210.

(21) Mu, L.; Feng, X.; Kou, R.; Zhang, Y.; Guo, H.; Tian, C.; Sun, C. J.; Du, X. W.; Nordlund, D.; Xin, H. L.; Lin, F. Deciphering the Cathode−Electrolyte Interfacial Chemistry in Sodium Layered Cathode Materials. *Adv. Energy Mater.* **2018**, *8*, 1801975.

(22) Li, Y.; Li, X.; Du, C.; Sun, H.; Zhang, Y.; Liu, Q.; Yang, T.; Zhao, J.; Delmas, C.; Harris, S. J.; Chen, H.; Huang, Q.; Tang, Y.; Zhang, L.; Zhu, T.; Huang, J. Degradation by Kinking in Layered Cathode Materials. *ACS Energy Lett.* **2021**, 3960−3969.
(23) Yang, T.; Zhao, Y. L.; Tong, Y.; Jiao, Z. B.; Wei, J.; Cai, J. X.; Han, X. D.; Chen, D.; Hu, A.; Kai, J. J.; Lu, K.; Liu, Y.; Liu, C. T. Multicomponent intermetallic nanoparticles and superb mechanical behaviors of complex alloys. *Science* **2018**, *362*, 933−937.
(24) Sarkar, A.; Velasco, L.; Wang, D.; Wang, Q.; Talasila, G.; de Biasi, L.; Kubel, C.; Brezesinski, T.; Bhattacharya, S. S.; Hahn, H.; Breitung, B. High entropy oxides for reversible energy storage. *Nat. Commun.* **2018**, *9*, 3400.
(25) Li, T.; Yao, Y.; Huang, Z.; Xie, P.; Liu, Z.; Yang, M.; Gao, J.; Zeng, K.; Brozena, A. H.; Pastel, G.; Jiao, M.; Dong, Q.; Dai, J.; Li, S.; Zong, H.; Chi, M.; Luo, J.; Mo, Y.; Wang, G.; Wang, C.; Shahbazian-Yassar, R.; Hu, L. Denary oxide nanoparticles as highly stable catalysts for methane combustion. *Nat. Catal.* **2021**, *4*, 62−70.
(26) Xu, H.; Zhang, Z.; Liu, J.; Do-Thanh, C. L.; Chen, H.; Xu, S.; Lin, Q.; Jiao, Y.; Wang, J.; Wang, Y.; Chen, Y.; Dai, S. Entropy-stabilized single-atom Pd catalysts via high-entropy fluorite oxide supports. *Nat. Commun.* **2020**, *11*, 3908.
(27) Zhao, C.; Ding, F.; Lu, Y.; Chen, L.; Hu, Y. S. High-Entropy Layered Oxide Cathodes for Sodium-Ion Batteries. *Angew. Chem., Int. Ed.* **2020**, *59*, 264−269.
(28) Lun, Z.; Ouyang, B.; Kwon, D. H.; Ha, Y.; Foley, E. E.; Huang, T. Y.; Cai, Z.; Kim, H.; Balasubramanian, M.; Sun, Y.; Huang, J.; Tian, Y.; Kim, H.; McCloskey, B. D.; Yang, W.; Clement, R. J.; Ji, H.; Ceder, G. Cation-disordered rocksalt-type high-entropy cathodes for Li-ion batteries. *Nat. Mater.* **2021**, *20*, 214−221.
(29) George, E. P.; Raabe, D.; Ritchie, R. O. High-entropy alloys. *Nat. Rev. Mater.* **2019**, *4*, 515−534.
(30) Zhao, C.; Wang, Q.; Yao, Z.; Wang, J.; Sanchez-Lengeling, B.; Ding, F.; Qi, X.; Lu, Y.; Bai, X.; Li, B.; Li, H.; Aspuru-Guzik, A.; Huang, X.; Delmas, C.; Wagemaker, M.; Chen, L.; Hu, Y. S. Rational design of layered oxide materials for sodium-ion batteries. *Science* **2020**, *370*, 708−711.
(31) Wu, Y.; Cao, C.; Zhu, Y.; Li, J.; Wang, L. Cube-shaped hierarchical $LiNi_{1/3}Co_{1/3}Mn_{1/3}O_2$ with enhanced growth of nanocrystal planes as high-performance cathode materials for lithium-ion batteries. *J. Mater. Chem. A* **2015**, *3*, 15523−15528.
(32) Xiao, Y.; Wang, P. F.; Yin, Y. X.; Zhu, Y. F.; Niu, Y. B.; Zhang, X. D.; Zhang, J.; Yu, X.; Guo, X. D.; Zhong, B. H.; Guo, Y. G. Exposing {010} Active Facets by Multiple-Layer Oriented Stacking Nanosheets for High-Performance Capacitive Sodium-Ion Oxide Cathode. *Adv. Mater.* **2018**, e1803765.
(33) Kim, U.-H.; Park, G.-T.; Son, B.-K.; Nam, G. W.; Liu, J.; Kuo, L.-Y.; Kaghazchi, P.; Yoon, C. S.; Sun, Y.-K. Heuristic solution for achieving long-term cycle stability for Ni-rich layered cathodes at full depth of discharge. *Nat. Energy* **2020**, *5*, 860−869.
(34) Yuan, D. D.; Wang, Y. X.; Cao, Y. L.; Ai, X. P.; Yang, H. X. Improved Electrochemical Performance of Fe-Substituted $Na-Ni_{0.5}Mn_{0.5}O_2$ Cathode Materials for Sodium-Ion Batteries. *ACS Appl. Mater. Interfaces* **2015**, *7*, 8585−8591.
(35) Hu, Z.; Weng, M.; Chen, Z.; Tan, W.; Li, S.; Pan, F. The role of $M@Ni_6$ superstructure units in honeycomb-ordered layered oxides for Li/Na ion batteries. *Nano Energy* **2021**, *83*, 105834.
(36) Xu, C.; Marker, K.; Lee, J.; Mahadevegowda, A.; Reeves, P. J.; Day, S. J.; Groh, M. F.; Emge, S. P.; Ducati, C.; Layla Mehdi, B.; Tang, C. C.; Grey, C. P. Bulk fatigue induced by surface reconstruction in layered Ni-rich cathodes for Li-ion batteries. *Nat. Mater.* **2021**, *20*, 84−92.
(37) Huang, J.; Zhong, P.; Ha, Y.; Kwon, D.-H.; Crafton, M. J.; Tian, Y.; Balasubramanian, M.; McCloskey, B. D.; Yang, W.; Ceder, G. Non-topotactic reactions enable high rate capability in Li-rich cathode materials. *Nat. Energy* **2021**, *6*, 706−714.
(38) Li, B.; Sougrati, M. T.; Rousse, G.; Morozov, A. V.; Dedryvere, R.; Iadecola, A.; Senyshyn, A.; Zhang, L.; Abakumov, A. M.; Doublet, M. L.; Tarascon, J. M. Correlating ligand-to-metal charge transfer with voltage hysteresis in a Li-rich rock-salt compound exhibiting anionic redox. *Nat. Chem.* **2021**, *13*, 1070−1080.
(39) Zhu, Z.; Yu, D.; Shi, Z.; Gao, R.; Xiao, X.; Waluyo, I.; Ge, M.; Dong, Y.; Xue, W.; Xu, G.; Lee, W.-K.; Hunt, A.; Li, J. Gradient-morph $LiCoO_2$ single crystals with stabilized energy density above 3400 W h L^{-1}. *Energy Environ. Sci.* **2020**, *13*, 1865−1878.
(40) Zhu, Z.; Gao, R.; Waluyo, I.; Dong, Y.; Hunt, A.; Lee, J.; Li, J. Stabilized Co-Free Li-Rich Oxide Cathode Particles with An Artificial Surface Prereconstruction. *Adv. Energy Mater.* **2020**, *10*, 2001120.
(41) Xu, G. L.; Amine, R.; Abouimrane, A.; Che, H.; Dahbi, M.; Ma, Z. F.; Saadoune, I.; Alami, J.; Mattis, W. L.; Pan, F.; Chen, Z.; Amine, K. Challenges in Developing Electrodes, Electrolytes, and Diagnostics Tools to Understand and Advance Sodium-Ion Batteries. *Adv. Energy Mater.* **2018**, *8*, 2003404.
(42) Hwang, J. Y.; Oh, S. M.; Myung, S. T.; Chung, K. Y.; Belharouak, I.; Sun, Y. K. Radially aligned hierarchical columnar structure as a cathode material for high energy density sodium-ion batteries. *Nat. Commun.* **2015**, *6*, 6865.
(43) Xie, Y.; Xu, G.-L.; Che, H.; Wang, H.; Yang, K.; Yang, X.; Guo, F.; Ren, Y.; Chen, Z.; Amine, K.; Ma, Z.-F. Probing Thermal and Chemical Stability of $Na_xNi_{1/3}Fe_{1/3}Mn_{1/3}O_2$ Cathode Material toward Safe Sodium-Ion Batteries. *Chem. Mater.* **2018**, *30*, 4909−4918.
(44) Shi, Y.; Zhang, Z.; Jiang, P.; Gao, A.; Li, K.; Zhang, Q.; Sun, Y.; Lu, X.; Cao, D.; Lu, X. Unlocking the potential of P3 structure for practical Sodium-ion batteries by fabricating zero strain framework for Na^+ intercalation. *Energy Storage Mater.* **2021**, *37*, 354−362.
(45) Mariyappan, S.; Wang, Q.; Tarascon, J. M. Will Sodium Layered Oxides Ever Be Competitive for Sodium Ion Battery Applications? *J. Electrochem. Soc.* **2018**, *165*, A3714−A3722.

https://doi.org/10.1021/jacs.2c02353
J. Am. Chem. Soc. XXXX, XXX, XXX−XXX